

Electrospun Ti-doped hematite fibres and their properties

Marko Robić • Mira Ristić • Marijan Marciuš • Stjepko Krehula • Svetozar Musić

Abstract Electrospun Ti-doped α -Fe₂O₃ fibres were synthesized and their properties compared with electrospun α -Fe₂O₃ and TiO₂ fibres as reference samples. All samples were characterized with FE SEM (Field Emission Scanning Electron Microscopy), XRD (X-ray Diffraction), ⁵⁷Fe Mössbauer, FT-IR (Fourier Transform Infrared) and UV/Vis/NIR (Ultraviolet/Visible/Near Infrared) techniques. Ti-doped α -Fe₂O₃ fibres consisted of the interconnected nanoparticles. These fibres showed a hollow substructure. XRD and ⁵⁷Fe Mössbauer spectroscopy showed the titanium cations to be incorporated up to 10 mol % into the α -Fe₂O₃ crystal structure. The incorporation of titanium cations into the α -Fe₂O₃ crystal structure caused changes in the corresponding FT-IR spectra. The band gap values of the electrospun fibres were determined and the photocatalytic degradation of rhodamine B (RhB) with the same fibres was investigated.

Keywords Ti-doped α -Fe₂O₃ · electrospinning · FE SEM · XRD · spectroscopy · photocatalysis

M. Robić¹ • M. Ristić¹ • M. Marciuš¹ • S. Krehula¹ • S. Musić^{1,2} (✉)

¹Division of Materials Chemistry, Rudjer Bošković Institute, P. O. Box 180, HR-10002, Zagreb, Croatia

²Croatian Academy of Sciences and Arts, Zrinski trg 11, HR-10000, Zagreb, Croatia

✉ E-mail: music@irb.hr

Introduction

In the last two decades a significant number of investigations appeared with the aim to find best materials for photoelectrochemical (PEC) water splitting or photocatalytic decontamination of polluted water. Hematite ($\alpha\text{-Fe}_2\text{O}_3$) was selected as a potential material for these applications due to several advantages. It has a suitable band gap value (~ 2.1 to 2.2 eV) and can absorb a large portion of the visible solar spectrum. Moreover, hematite is characterized by good chemical stability over a broad pH range in the aqueous medium, nontoxicity and a relatively low cost. Naturally occurring hematite can also be used as a photocatalyst, due to its abundance in nature. However, synthetic hematites showed the best results in the photocatalytic activity.

Ti-doped $\alpha\text{-Fe}_2\text{O}_3$ was investigated as a promising photoanode in photoelectrochemical water splitting. Wang et al. [1] used the hydrothermal method combined with thermal annealing to prepare $\alpha\text{-Fe}_2\text{O}_3$ and Ti-doped $\alpha\text{-Fe}_2\text{O}_3$ nanorod arrays on FTO (Fluorine-doped Tin Oxide) glass. A similar investigation was conducted by Su et al. [2]. It was also found that Ti-doped $\alpha\text{-Fe}_2\text{O}_3$ coated with $\text{Ni}(\text{OH})_2$ [3] or InOOH [4] enhanced the PEC (Photoelectrochemical) activity of these materials. Yang et al. [5] prepared the arrays of Ti-doped $\alpha\text{-Fe}_2\text{O}_3$ particles on undoped $\alpha\text{-Fe}_2\text{O}_3$ as a layer on the FTO substrate. $\beta\text{-FeOOH}$ branched nanorods were orthogonal onto the Ti-doped Fe_2O_3 surface. Mazzaro et al. [6] reported a possible utilization of Ti-doped $\alpha\text{-Fe}_2\text{O}_3$ in the simultaneous photoinduced oxidation of benzylamine to N-benzylidenbenzylamine and hydrogen (H_2) production. Toussaint et al. [7] investigated Ti-doped $\alpha\text{-Fe}_2\text{O}_3$ mesoporous films for a possible application as photoanodes in the photoelectrolysis of water. The preservation of a porous microstructure enabled a better electrolyte penetration in the film and thus reduced the distance that the photogenerated holes had to travel to reach the electrolyte. Bu et al. [8] incorporated ferrihydrite as a whole transfer channel between Ti-doped $\alpha\text{-Fe}_2\text{O}_3$ and cobalt phosphate and reported that superior photocurrent density was achieved. Kang and Kang [9] found that the incorporation of an ultrathin SiO_2 layer between the FTO substrate and Ti-doped $\alpha\text{-Fe}_2\text{O}_3$ film suppressed a reverse electron recombination from the FTO substrate to the Ti-doped $\alpha\text{-Fe}_2\text{O}_3$ layer, thus enhancing the PEC activity in water splitting. Furthermore, the atmospheric pressure chemical vapour deposition [10], pulsed laser deposition [11] and the electrospraying method [12] were used in the preparation of Ti-doped films. Santangelo et al.

[13] deposited Ti-doped α -Fe₂O₃ and Si-doped γ -Fe₂O₃ fibres on the ITO glass substrate using the electrospinning method and measured their photoelectrochemical efficiencies.

This short selection from the works about Ti-doped α -Fe₂O₃ showed a diversity of approaches to the synthesis of this material as well as the corresponding characterisations. In the present work we report the formation of Ti-doped α -Fe₂O₃ fibres for different amounts of Ti-dopant using electrospinning as the synthesis method. Electrospinning is a unique method in the synthesis of various nanofibres which found application in science, engineering and biomedicine [14]. Additionally, the electrospun α -Fe₂O₃ and TiO₂ fibres, as reference samples, were prepared to compare their microstructural and photocatalytic properties with those of Ti-doped hematite fibres. The photocatalytic activities of prepared samples were tested using the degradation of rhodamine B.

Experimental

Preparation of samples

Ti (IV)-isopropoxide (TIP, 97+%, CAS 546-68-9), Fe(NO₃)₃•9H₂O (98+%, CAS 7782-61-8) and polyvinylpyrrolidone (PVP, M_w= 1 300 000, CAS 9003-39-8) were supplied by *Alfa Aesar*[®]. Absolute ethanol p.a. (CAS 64-17-5) and 30 % H₂O₂ (CAS 7722-84-1) were supplied by *Kemika* (Zagreb, Croatia). Glacial acetic acid, p.a. (CAS 64-19-7) was supplied by *Alkaloid* (Skopje, North Macedonia). Rhodamine B, p.a. (RhB, CAS 107599) by *Merck* was used. Mili-Q water was used. Chemical conditions for the preparation of samples Ti0 (no titanium), Ti5 (5 mol % Ti), Ti10 (10 mol % Ti) and Ti100 (no iron) are given in Table 1.

Ti (IV)-isopropoxide 1M solution (a) was prepared by adding a proper amount of this chemical into the volumetric flask. Then 2-propanol was added to the mark of 25 mL total volume. Iron (III)-nitrate 1M solution (b) was prepared by dissolving 10.307g of Fe(NO₃)₃•9H₂O salt in mili-Q water also using a 25 mL volumetric flask. PVP in the C₂H₅OH viscous solution (c) was prepared by dissolving 5g of this polymer into the 50 mL volumetric flask. The viscous solution was mixed at 70°C and 350 rpm for 3h. Proper amounts of C₂H₅OH/glacial acetic acid/or water were additionally added into corresponding volumes of the (a) TIP solution (for Ti100 synthesis), (b) Fe(NO₃)₃•9H₂O solution (for Ti0 synthesis) or their (a,b) mixtures (for Ti5 and Ti10 synthesis) (Table 1). The electrospinning solutions were prepared by slow adding (during 5 min) each of these three solutions into a previously prepared viscous PVP solution (c).

This adding was conducted under strong mixing (350 rpm). A similar synthesis of SnO₂ /TiO₂ composite nanofibres was used by Tran et al [15].

The electrospinning device was set up using a Harvard Apparatus (Pump11 elite) and a high-voltage auto-reserving power supply CZE1000R manufactured by *Spellman* (N.Y., USA). The metallic nozzle was connected to the positive terminal of the power supply source and the voltage was adjusted to 20 kV. The negative end was grounded and connected to the aluminium plate sized 15×20 cm. This aluminium plate was covered with a thick aluminium foil (0.030 mm) for collecting the electrospun material. The distance between the metallic nozzle tip (needle 21G) and the aluminium plate was 10 cm. The electrospinning process was conducted at a flow rate of 25 µL/min. No more than 5 mL of the electrospinning solution was electrospun on a single aluminium foil. The process was repeated and a few batches were produced. Thus prepared electrospun fibres on aluminium foil were put in vacuum for at least 15h at RT. Each individual electrospun batch (without aluminium foil) was put in its separate Al₂O₃ crucible. Fibre mats were then heated in the laboratory oven. Temperature in the oven was gradually increased by 10°C/min up to 550°C and after 3h of heating the crucibles were taken out of the furnace and left cooling to RT.

Instrumentation

FE SEM images of prepared samples were taken with a scanning electron microscope JSM 7000F manufactured by *JEOL Ltd.* linked to the EDS/INCA 350 (energy dispersive X-ray analyzer) manufactured by *Oxford Instruments*.

XRD patterns were recorded at RT with a *Panalytical Aeris* powder diffractometer using CuK $\alpha_{1,2}$ radiation. In the evaluation of XRD patterns, the programs Match! and Dicvol06 were used.

Mössbauer spectra were recorded at RT using a spectrometer set up with modules supplied by *Wissenschaftliche Elektronik GmbH*. ⁵⁷Co/Rh was used as a Mössbauer source. The Mössbauer spectrometer was calibrated with α -Fe. The recorded Mössbauer spectra were evaluated with the *MossWinn* computer program.

UV/Vis spectra were recorded with a *Shimadzu 3600* spectrometer linked to an integrating sphere. The samples were put on top of BaSO₄ powder (*Wako Chemicals*) spread on the surface, then pressed into a holder.

FT-IR spectra were recorded using a spectrometer Frontier manufactured by *Perkin Elmer*.

The photocatalytic measurements were conducted with a MAX-303-Compact Xenon Light source with a 300 W lamp manufactured by *Asahi Spectra* and the corresponding filter. The suspension containing Ti-doped α -Fe₂O₃ catalyst, RhB and H₂O₂ was illuminated in the range of visible light ($420 \text{ nm} < \lambda < 700 \text{ nm}$) up to 3h. The standard procedure for photocatalytic experiments was reported elsewhere [16]. The errors are estimated with the last significant digit.

Results and Discussion

Figures 1 and 2 show FE SEM images at different optical magnification of electrospun Ti0 to Ti100 produced by heating the precursor (composite) fibres at 550°C for 3h. In all cases well-developed fibres are visible. Ti-doped α -Fe₂O₃ fibres (samples Ti5 and Ti10) showed a well visible substructure, i.e., the interconnected nanosize particles as the forming units in these fibres (Figure 2).

Figure 3 shows broken Ti5 and Ti10 fibres as grinded with spatula, and their hollow substructure. During the heating of precursor (composite) fibres a solid outer layer of interconnected nanosize Ti-doped α -Fe₂O₃ was formed first. We assume that the released gases originating from organic components and nitrates in bulk (deposit/precipitate) to be under pressure, thus enabling the formation of a hollow substructure. The formation of hollow structures in metal oxides (nanofibers and nanotubes) was the subject of investigations by many researchers [17-22]. However, this problem is not solved with general conclusion. This is understandable, because the appearance of hollow nanofibers and nanotubes strongly depends on the nature of chemical compounds (precursors) and the preparation procedures. Figure 4 shows for illustration the mapping of sample Ti10. The atoms Fe, Ti and O are well distributed at/near the surface of this sample.

Figure 5 shows the XRD patterns of samples Ti0 (no titanium), Ti5 (5 mol % Ti), Ti10 (10 mol % Ti) and Ti100 (no iron). The diffraction lines of reference hematite, rutile and anatase are identified on the basis of powder diffraction data in JCPDS powder diffraction file (card No. 00-033-0664 for hematite; cards Nos. 00-021-1272 and 00-021-1276 for anatase and rutile, respectively). The XRD pattern of sample Ti0 corresponds to hematite as a single phase, whereas sample Ti100 is a mixture of rutile and anatase. The XRD patterns of samples Ti5 and Ti10 correspond structurally to a hematite phase. The unit-cell parameters calculated for samples Ti0, Ti5 and Ti10 are given in Table 2. The unit-cell volume decreased slightly with the increase in

structurally incorporated titanium cations. The crystallite size of the corresponding particles decreased in the order Ti0, Ti5 and Ti10.

Figure 6a shows the RT Mössbauer spectra of reference sample Ti0 and samples Ti5 and Ti10 which are characterized with one sextet of Mössbauer lines corresponding to the hematite phase. In the spectrum of sample Ti10 a central quadrupole doublet of small relative intensity is noticed and taking into account XRD results it can be assigned to a small fraction of superparamagnetic particles (5.8 %). The Mössbauer spectra of these samples were fitted using the distribution of hyperfine magnetic fields (B_{hf}) shown in Figure 6b. The calculated Mössbauer parameters are given in Table 3. A reduction in the hyperfine magnetic field (B_{hf}) and a slight increase of the linewidth (Γ) are visible due to the incorporation of Ti^{4+} cations into the hematite crystal structure.

Figure 7 shows the FT-IR spectra of samples Ti0 to Ti100. Sample Ti0 (no titanium) shows two very strong IR bands at 520 and 438 cm^{-1} , one small intensity IR band at 387 cm^{-1} , as well as two shoulders at 650 and 590 cm^{-1} . This FT-IR spectrum can be assigned to the $\alpha-Fe_2O_3$ phase. Generally, the IR spectrum of $\alpha-Fe_2O_3$ shows six active vibrations, two $A_{2u}(E||c)$ and four $E_u(E\perp c)$. The parameters (ω_T and ω_L) obtained by a harmonic oscillator model, as applied to $\alpha-Fe_2O_3$, are reported in reference literature [23-26]. Two shoulders at 650 and 590 cm^{-1} which appeared in the FT-IR spectrum of sample Ti0 can be related to the nano/micro structure of long $\alpha-Fe_2O_3$ fibres. Rendon and Serna [27] reported a significant difference in the IR spectra of $\alpha-Fe_2O_3$ in dependence on the size and shape of the corresponding particles. In the FT-IR spectra of samples Ti5 and Ti10 the shoulder at 590 cm^{-1} as well as a small intensity IR band at 387 cm^{-1} diminished as a direct consequence of the incorporation of Ti^{4+} cations into the crystal structure of $\alpha-Fe_2O_3$. The FT-IR spectrum of sample Ti100 (no iron) is characterized with one strong IR band at 488 cm^{-1} , two very broad shoulders positioned at 738 and 574 cm^{-1} and one IR band close to 375 cm^{-1} . Since the XRD pattern of this sample showed the presence of rutile as the dominant phase associated with the anatase phase, the FT-IR spectrum of sample Ti100 can be considered as the contribution of these two TiO_2 polymorphs. Posch et al. [28] reported IR bands for both tetragonal rutile and anatase, which are close to the IR bands shown for sample Ti100. Ocaña et al. [29] reported that the particle size and the state of aggregation of TiO_2 (rutile) show a strong impact on the IR spectrum, as theoretically predicted. The Raman spectra additionally

showed changes at the surface of rutile particles. Gonzalez et al. [30] reported data for transverse optical (TO) and longitudinal optical (LO) frequencies (in cm^{-1}) for the anatase polymorph.

Figure 8 shows UV/Vis/NIR spectra recorded for samples Ti0 to Ti100. The electrospun $\alpha\text{-Fe}_2\text{O}_3$ fibres (sample Ti0) are characterized with very small relative intensity bands at 340 and 459 nm, shoulders at 541 and 673 nm as well as two shoulders at 827 and 880 nm. The most pronounced effect of Ti-doping is visible on a shift of the band at 827 to 855 nm and a relative increase in the intensity of the band at 855 nm. The nature of UV/Vis/NIR bands recorded for $\alpha\text{-Fe}_2\text{O}_3$ was discussed in reference literature [31, 32]. It is generally known that the procedure of $\alpha\text{-Fe}_2\text{O}_3$ doping with various metal cations affects the nano/micro structure of $\alpha\text{-Fe}_2\text{O}_3$, the optical spectra, as well as some other properties. This was illustrated by Ristić et al. [31]. In a mentioned work [31], Mn-doped 1D goethite ($\alpha\text{-FeOOH}$) particles were prepared by the coprecipitation method starting with NaOH and iron choline citrate solutions. Thus formed Mn-doped $\alpha\text{-FeOOH}$ particles were heated at 300°C to obtain Mn-doped 1D $\alpha\text{-Fe}_2\text{O}_3$ particles. Malviya et al. [33] prepared thin films of Ti-doped $\alpha\text{-Fe}_2\text{O}_3$ on an FTO-coated soda lime glass substrate with a varying amount of titanium up to 7%. The UV/Vis spectra were recorded and the photoelectrochemical effect was investigated with these films.

The UV/Vis spectrum of sample Ti100 is characterized with one broad band of a very strong intensity corresponding to TiO_2 polymorphs (~ 3.2 eV for anatase and brookite and ~ 3.0 for rutile were reported). In the solar spectrum UV radiation participates only by a few percent, whereas the rest are visible and infrared radiation. For this reason researchers are trying to shift the absorption for TiO_2 more towards the visible part of the spectrum [34]. Serpone [35] discussed the doping of TiO_2 with either anions (mostly N, C, and S) or cations in order to enhance the photonic efficiencies of photoassisted surface redox reactions. Khan et al. [36] reported the enhanced photocatalytic and photoelectrochemical activities of TiO_2 previously irradiated with an electron beam. Ansari and Cho [37] achieved similar effects by ball-milling TiO_2 with elemental phosphorus. Hu et al. [38] investigated the photocatalytic properties of a composite, electrospun TiO_2 / MWNT (MWNT= multi-walled nanotubes). These works showed that the composition and preparation procedure play a very important role in the photocatalytic and photoelectrochemical properties of TiO_2 . Generally, anatase is a more active photocatalyst than the rutile polymorph [39]. Investigating this feature, Luttrell et al. [40] concluded that the bulk transport of excitons to the surface contributes to this difference. It was found that for

anatase the activity increases for films up to ~5 nm thick, whereas for rutile films the maximum activity is up to ~2.5 nm. This showed that charge carriers excited deeper in the bulk contribute more to the surface reactions in anatase than in rutile.

Figure 9 shows direct band gaps (E_g / eV) of samples Ti0, Ti5 and Ti10 as determined by the Tauc plot method. In this figure the linear parts of curves are shown in shadow and the corresponding linear plots are intersected by the x-axis to obtain E_g / eV values. It is visible that the incorporation of titanium into the α -Fe₂O₃ crystal structure caused a decrease in E_g values from 2.13 eV for sample Ti0 to 2.06 for sample Ti10.

Fig. 10 shows the kinetics of photocatalytic degradation of RhB in the solutions containing H₂O₂. The numeric data for these kinetics (up to 3h) are given in Table 4. It is well visible that the best photocatalytic activity was obtained for reference sample Ti0 (94 %). Doping of α -Fe₂O₃ with 5% titanium reduced the photocatalytic activity to 28 % (sample Ti5), then with a further increase of titanium (sample Ti10) the photocatalytic activity increased in relation to sample Ti5. The medium photocatalytic activity (54 %) was obtained for sample Ti100 (no iron). This work undoubtedly showed that the incorporation of titanium cations into the α -Fe₂O₃ structure significantly impaired the photocatalytic efficacy of the corresponding samples (Ti5 and Ti10). Here, taking into account reference literature (see Introduction) it can be emphasized that, contrary to present photocatalytic experiments, the photoelectrochemical (PEC) efficacy is higher when Ti-doped α -Fe₂O₃ is used instead of undoped α -Fe₂O₃. Probably these differences are due to some specific reactions involved in the photocatalytic degradation of RhB and photoelectrochemical behaviour of Ti-doped α -Fe₂O₃.

Incorporation of Ti⁴⁺ cations into the hematite crystal structure caused defects due to different charges of Ti⁴⁺ and Fe³⁺. This was accompanied with a slight changes in the band gap values from 2.13 to 2.06 eV for samples Ti0 to Ti10. An abrupt decrease in photocatalytic activity of sample Ti5 was noticed. The increase of photocatalytic activity of sample Ti10 can be related with the increase of the amount of Ti⁴⁺ cations at/near the surface of Ti-doped hematite particles (preconcentration effect).

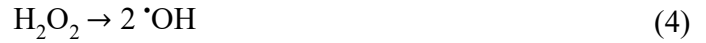
The complexity of problem can be illustrated with the following works. Investigation of the electrospun BN/TiO₂ (BN=boron nitride) composite nanofibers showed significantly high photocatalytic activity (99%) in relation to commercial P25 powder (60%) and TiO₂ nanofibres (65%) [41]. Nasr et al. [42] showed that electrospun BN-Ag/TiO₂ composite nanofibers also

showed a high photocatalytic activity, which was assigned to the efficient electron transfer from photoexcited Ag/TiO₂ to BN nanosheets to retard TiO₂ charge recombination. BN5-Ag3/TiO₂ composite was selected as efficient and long term stable antibacterial material for biomedicine use and water disinfection. These works also showed the complexity of photocatalytic activity of metal oxide materials and corresponding dependence on the chemical composition and synthetic procedure applied.

Photocatalytic reactions involved during the irradiation of metal oxides in an aqueous medium with solar light can [43, 44] also be applied to hematite or a Ti-doped hematite photocatalyst. This photocatalytic process starts with the formation of hole-electron pairs as follows:



where VB is a valence band and CB is a conduction band. Due to the charge separation the following oxidative and reductive reactions are possible taking into account h^+ and e^- , respectively.



The hydroxyl ($\cdot OH$) and superoxide ($\cdot O_2^-$) radicals are supposed to be the most reactive species [45, 46]. Generally, the efficacy of oxidative (h^+) and reductive (e^-) photocatalytic reactions depends on several factors such as the band gap, presence of different metal cation dopants, crystal defects, size and morphology of particles or films, penetration of solar light into the metal oxide as well as the recombination of charges. These facts show a very complex nature of photocatalytic processes involving metal oxide materials.

Conclusions

Electrospun Ti-doped α -Fe₂O₃ fibres containing up to 10 mol % titanium cations were synthesized. Upon calcination of the composite fibres at 550°C, the obtained Ti-doped α -Fe₂O₃ fibres consisted of the interconnected nanosize particles. These fibres showed a hollow substructure. XRD patterns confirmed the presence of an α -Fe₂O₃ crystal structure with up to 10 mol % Ti⁴⁺ ions incorporated. The incorporation of Ti⁴⁺ ions into α -Fe₂O₃ fibres was also confirmed by Mössbauer spectroscopy measuring the reduction of hyperfine magnetic fields in relation to reference α -Fe₂O₃ fibres. The effect of the incorporation of titanium cations into the α -Fe₂O₃ crystal structure was also noticed in the FT-IR spectra. Band gap values of the samples were determined using the UV/Vis spectra and the Tauc plot method. The incorporation of 5 mol % titanium cations into the α -Fe₂O₃ structure significantly reduced the photocatalytic degradation of rhodamine B (RhB). The photocatalytic effect increased for 10 mol % titanium cations incorporated. These measurement show the difference between the behaviour of electrospun Ti-doped α -Fe₂O₃ nanofibres in the degradation of RhB on one side and the photoelectrochemical effect of Ti-doped α -Fe₂O₃ nanoparticles or nanofilms in water splitting (see Introduction) on the other.

Acknowledgment This research has been supported by the Croatian Science Foundation (Project number IP-2016-06-8254).

Conflict of interest The authors declare that they have no conflict of interest.

References

1. Wang Q, Chen Y, Xu J, Situ Y, Huang H (2018) Morphology-controlled synthesis of Ti-doped α -Fe₂O₃ nanorod arrays as an efficient photoanode for photoelectrochemical applications. *Res Chem Intermed* 44:2365–2378. <https://doi.org/10.1007/s11164-017-3234-7>
2. Su J, Zhou J, Zong S, Zhou Z, Liu C, Feng B (2016) The effect of thermal annealing on the interfacial properties and photoelectrochemical performance of Ti doped Fe₂O₃ nanowire arrays. *RSC Adv* 6:99851–99858. <https://doi.org/10.1039/c6ra19699c>
3. Li Q, Bian J, Zhang N, Ng DHL (2015) Loading Ni(OH)₂ on the Ti-doped hematite photoanode for photoelectrochemical water splitting. *Electrochim Acta* 155:383–390. <https://doi.org/10.1016/j.electacta.2014.12.131>
4. Zhang S, Shangguan P, Tong S, Zhang Z, Leng W (2020) Correction to “Enhanced photoelectrochemical oxidation of water over Ti doped α -Fe₂O₃ electrodes by surface electrodeposition InOOH”. *J Phys Chem C* 124:4925–4925. <https://doi.org/10.1021/acs.jpcc.0c00922>
5. Yang TY, Kang HY, Jin K, Park S, Lee JH, Sim U, Jeong HY, Joo YC, Nam KT (2014) An iron oxide photoanode with hierarchical nanostructure for efficient water oxidation. *J Mater Chem A* 2:2297–2305. <https://doi.org/10.1039/c3ta13830e>
6. Mazzaro R, Boscolo Bibi S, Natali M, Bergamini G, Morandi V, Ceroni P, Vomiero A (2019) Hematite nanostructures: An old material for a new story. Simultaneous photoelectrochemical oxidation of benzylamine and hydrogen production through Ti doping. *Nano Energy* 61:36–46. <https://doi.org/10.1016/j.nanoen.2019.04.013>
7. Toussaint C, Tran HL Le, Colson P, Dewalque J, Vertruyen B, Gilbert B, Nguyen ND, Cloots R, Henrist C (2015) Combining mesoporosity and Ti-doping in hematite films for water splitting. *J Phys Chem C* 119:1642–1650. <https://doi.org/10.1021/jp5091476>
8. Bu Q, Li S, Zhang K, Lin Y, Wang D, Zou X, Xie T (2019) Hole transfer channel of ferrihydrite designed between Ti-Fe₂O₃ and CoPi as an efficient and durable photoanode. *ACS Sustain Chem Eng* 7:10971–10978. <https://doi.org/10.1021/acssuschemeng.9b02009>
9. Kang MJ, Kang YS (2015) Ultrathin insulating under-layer with a hematite thin film for enhanced photoelectrochemical (PEC) water splitting activity. *J Mater Chem A* 3:15723–15728. <https://doi.org/10.1039/c5ta03468j>
10. Zhang P, Kleiman-Shwarstein A, Hu YS, Lefton J, Sharma S, Forman AJ, McFarland E

- (2011) Oriented Ti doped hematite thin film as active photoanodes synthesized by facile APCVD. *Energy Environ Sci* 4:1020–1028. <https://doi.org/10.1039/c0ee00656d>
11. Atabaev TS, Ajmal M, Hong NH, Kim HK, Hwang YH (2014) Ti-doped hematite thin films for efficient water splitting. *Appl Phys A Mater Sci Process* 118:1539–1542. <https://doi.org/10.1007/s00339-014-8937-7>
 12. Chae SY, Rahman G, Joo O (2019) Elucidation of the structural and charge separation properties of titanium-doped hematite films deposited by electrospray method for photoelectrochemical water oxidation. *Electrochim Acta* 297:784–793. <https://doi.org/10.1016/j.electacta.2018.11.166>
 13. Santangelo S, Frontera P, Pantò F, Stelitano S, Marelli M, Patane S, Malara F, Santo VD, Antonucci P (2017) Effect of Ti- or Si-doping on nanostructure and photo-electro-chemical activity of electro-spun iron oxide fibres. *Int J Hydrogen Energy* 42:28070–28081. <https://doi.org/10.1016/j.ijhydene.2017.03.204>
 14. Ramakrishna S, Fujihara K, Teo WE, Lim TC, Ma Z (2005) An introduction to electrospinning and nanofibers. World Scientific Publishing Co., Pte. Ltd., Singapore
 15. Tran T, McCormac K, Li J, Bi Z, Wu J (2014) Electrospun SnO₂ and TiO₂ composite nanofibers for lithium ion batteries. *Electrochim Acta* 117:68–75. <https://doi.org/10.1016/j.electacta.2013.11.101>
 16. Robić M, Ristić M, Marciuš M, Krehula S, Musić S (2020) Synthesis and properties of nanostructured Cr-doped hematite fibres. *Chem Pap.* 74:4345-4353. <https://doi.org/10.1007/s11696-020-01247-6>
 17. Barhoum A, Pal K, Rahier H, Uludag H, Kim IS, Bechelany M (2019) Nanofibers as new-generation materials: From spinning and nano-spinning fabrication techniques to emerging applications. *Appl. Materials Sci* 17:1-35. <https://doi.org/10.1016/j.apmt.2019.06.015>
 18. Nada AA, Nasr M, Viter R, Miele P, Roualdes S, Bechelany M (2017) Mesoporous ZnFe₂O₄@TiO₂ nanofibers prepared by electrospinning coupled to PECVD as highly performing photocatalytic materials. *J. Phys.Chem.* 121:24669-24677. <https://doi.org/10.1021/acs.jpcc.7b08567>
 19. Yang G, Yan W, Wang J, Yang H (2014) Fabrication and formation mechanism of Mn₂O₃ hollow nanofibers by single-spinneret electrospinning. *CrystEngComm* 16:6907-6913. <https://doi.org/10.1039/c4ce00521j>

20. Xia X, Dong XJ, Wei QF, Cai YB, Lu KY (2012) Formation mechanism of porous hollow SnO₂ nanofibers prepared by one-step electrospinning, *eXPRESS Polymer Letters* 6:169-176. <https://doi.org/10.3144/expresspolymlett.2012.18>
21. Tang H, Yao S, Jing M, Qian X, Shen X, Xi X (2014) Fabrication and characterization of Mg_{0.6}Ni_{0.4}O hollow nanofibres by electrospinning. *J. Nanosci. Nanotechnol.* 16:6414-6418. <https://doi.org/10.1166/jnn.2016.11042>
22. Einert M, Ostermann R, Weller T, Zellmer S, Garnweitner G, Smarsly BM, Marschall R (2016) Hollow α -Fe₂O₃ nanofibres for solar water oxidation: improving the photoelectrochemical performance by formation of α -Fe₂O₃/ITO-composite photoanodes, *Mater. Chem. A* 4:18444-18456. <https://doi.org/10.1039/C6TA06979G>
23. Onari S, Arai T, Kudo K (1977) Infrared lattice vibrations and dielectric dispersion in α -Fe₂O₃. *Phys Rev B* 16:1717–1721. <https://doi.org/10.1103/PhysRevB.16.1717>
24. Serna CJ, Ocana M, Iglesias JE (1987) Optical properties of α -Fe₂O₃ microcrystals in the infrared. *J Phys C Solid State Phys* 20:473–484. <https://doi.org/10.1088/0022-3719/20/3/017>
25. Wang Y, Muramatsu A, Sugimoto T (1998) FTIR analysis of well-defined α -Fe₂O₃ particles. *Colloids Surfaces A Physicochem Eng Asp* 134:281–297. [https://doi.org/10.1016/S0927-7757\(97\)00102-7](https://doi.org/10.1016/S0927-7757(97)00102-7)
26. Serna CJ, Rendon JL, Iglesias JE (1982) Infrared surface modes in corundum-type microcrystalline oxides. *Spectrochim Acta Part A Mol Spectrosc* 38:797–802. [https://doi.org/10.1016/0584-8539\(82\)80070-6](https://doi.org/10.1016/0584-8539(82)80070-6)
27. Rendon JL, Serna CJ (1981) IR spectra of powder hematite: effects of particle size and shape. *Clay Miner* 16:375–382. <https://doi.org/10.1180/claymin.1981.016.4.06>
28. Posch T, Kerschbaum F, Fabian D, Mutschke H, Dorschner J, Tamanai A, Henning T (2003) Infrared properties of solid titanium oxides: exploring potential primary dust condensates. *Astrophys J Suppl Ser* 149:437–445. <https://doi.org/10.1086/379167>
29. Ocaña M, Fornés V, Ramos JVG, Serna CJ (1988) Factors affecting the infrared and Raman spectra of rutile powders. *J Solid State Chem* 75:364–372. [https://doi.org/10.1016/0022-4596\(88\)90176-4](https://doi.org/10.1016/0022-4596(88)90176-4)
30. Gonzalez R, Zallen R, Berger H (1997) Infrared reflectivity and lattice fundamentals in anatases. *Phys Rev B - Condens Matter Mater Phys* 55:7014–7017. <https://doi.org/10.1103/PhysRevB.55.7014>

31. Ristić M, Kuzmann E, Homonnay Z, Musić S (2018) Synthesis and properties of 1D manganese-doped hematite particles. *J Alloys Compd* 767:504–511. <https://doi.org/10.1016/j.jallcom.2018.07.115>
32. Kleiman-Shwarsstein A, Hu YS, Forman AJ, Stucky GD, McFarland EN (2008) Electrodeposition of α -Fe₂O₃ doped with Mo or Cr as photoanodes for photocatalytic water splitting. *J Phys Chem C* 112:15900–15907. <https://doi.org/10.1021/jp803775j>
33. Malviya KD, Klotz D, Dotan H, Shlenkevich D, Tsyganok A, Mor H, Rothschild A (2017) Influence of Ti doping levels on the photoelectrochemical properties of thin-Film hematite (α -Fe₂O₃) photoanodes. *J Phys Chem C* 121:4206–4213. <https://doi.org/10.1021/acs.jpcc.7b00442>
34. Kumar SG, Devi LG (2011) Review on modified TiO₂ photocatalysis under UV/visible light: Selected results and related mechanisms on interfacial charge carrier transfer dynamics. *J Phys Chem A* 115:13211–13241. <https://doi.org/10.1021/jp204364a>
35. Serpone N (2006) Is the band gap of pristine TiO₂ narrowed by anion- and cation-doping of titanium dioxide in second-generation photocatalysts? *J Phys Chem B* 110:24287–24293. <https://doi.org/10.1021/jp065659r>
36. Khan MM, Ansari SA, Pradhan D, Ansari MO, Han DH, Lee J, Cho MH (2014) Band gap engineered TiO₂ nanoparticles for visible light induced photoelectrochemical and photocatalytic studies. *J Mater Chem A* 2:637–644. <https://doi.org/10.1039/c3ta14052k>
37. Ansari SA, Cho MH (2016) Highly visible light responsive, narrow band gap TiO₂ nanoparticles modified by elemental red phosphorus for photocatalysis and photoelectrochemical applications. *Sci Rep* 6:1–10. <https://doi.org/10.1038/srep25405>
38. Hu G, Meng X, Feng X, Ding Y, Zhang S, Yang M (2007) Anatase TiO₂ nanoparticles/carbon nanotubes nanofibers: Preparation, characterization and photocatalytic properties. *J Mater Sci* 42:7162–7170. <https://doi.org/10.1007/s10853-007-1609-7>
39. Luttrell T, Halpegamage S, Sutter E, Batzill M (2014) Photocatalytic activity of anatase and rutile TiO₂ epitaxial thin film grown by pulsed laser deposition. *Thin Solid Films* 564:146–155. <https://doi.org/10.1016/j.tsf.2014.05.058>
40. Luttrell T, Halpegamage S, Tao J, Kramer A, Sutter E, Batzill M (2014) Why is anatase a better photocatalyst than rutile? - Model studies on epitaxial TiO₂ films. *Sci Rep* 4:4043. <https://doi.org/10.1038/srep04043>
41. Nasr M, Viter R, Eid C, Habchi R, Miele P, Bechelany M (2017) Enhanced photocatalytic

performance of novel electrospun BN/TiO₂ composite nanofibers. *New J.Chem.* 41:81-89.
<https://doi.org/10.1039/c6nj03088b>

42. Nasr M, Soussan L, Viter R, Eid C, Habchi R, Miele P, Bechelany M (2018) High photodegradation and antibacterial activity of BN-Ag/TiO₂ composite nanofibers under visible light. *New J. Chem.* 42:1250-1259. <https://doi.org/10.1039/c7nj03183a>
43. Daneshvar N, Salari D, Khataee AR (2004) Photocatalytic degradation of azo dye acid red 14 in water on ZnO as an alternative catalyst to TiO₂. *J Photochem Photobiol A Chem* 162:317–322. [https://doi.org/10.1016/S1010-6030\(03\)00378-2](https://doi.org/10.1016/S1010-6030(03)00378-2)
44. Ong CB, Ng LY, Mohammad AW (2018) A review of ZnO nanoparticles as solar photocatalysts: Synthesis, mechanisms and applications. *Renew Sustain Energy Rev* 81:536–551. <https://doi.org/10.1016/j.rser.2017.08.020>
45. Cha HG, Noh HS, Kang MJ, Kang YS (2013) Photocatalysis: Progress using manganese-doped hematite nanocrystals. *New J Chem* 37:4004–4009. <https://doi.org/10.1039/c3nj00478c>
46. Rajeswari P, Dhanuskodi S, Jothi Venkatachalam K (2018) Impact of microwave-assisted synthesis on the morphology and rhodamine B oxidation properties of ZnO nanocomposites. *Appl Nanosci* 8:645–654. <https://doi.org/10.1007/s13204-018-0769-x>

Figure Legends

- Figure 1 FE SEM images of samples Ti0, Ti5, Ti10 and Ti100 at lower optical magnification
- Figure 2 FE SEM images of samples Ti0, Ti5, Ti10 and Ti100 at higher optical magnification
- Figure 3 FE SEM images of samples Ti5 and Ti10 showing the hollow substructure
- Figure 4 Distributions of iron, titanium and oxygen atoms illustrated with sample Ti10
- Figure 5 XRD patterns of the samples Ti0 (no titanium), Ti5 (5 mol % Ti), Ti10 (10 mol % Ti) and Ti100 (no iron). Standard XRD patterns of hematite, rutile and anatase are also shown
- Figure 6 (a) RT Mössbauer spectra of reference sample Ti0 and doped samples Ti5 and Ti10; (b) distributions of hyperfine magnetic fields (B_{hf}) for the same samples
- Figure 7 FT-IR spectra of samples Ti0 to Ti100
- Figure 8 UV/Vis/NIR spectra of samples Ti0 to Ti100
- Figure 9 Tauc plot method was used to determine direct band gaps (E_g / eV). The linear parts in curves are shown in shadow
- Figure 10 Photocatalytic efficiency in degradation of rhodamine B (c/c_0 vs. time of illumination) as determined for samples Ti0 to Ti100

Table 1

Chemical conditions for the preparation of samples

Samples	Ti0	Ti5	Ti10	Ti100
Solution (a, b)				
(a) 1M TIP in 2-propanol / mL		0.182	0.364	3.630
(b) 1M Fe(NO ₃) ₃ • 9H ₂ O in water / mL	3.630	3.448	3.266	
C ₂ H ₅ OH / mL	3	3	3	3
Glacial acetic acid / mL	1	1	1	1
Solution				
(c) PVP/C ₂ H ₅ OH / mL	10	10	10	10
Glacial acetic acid / mL	2	2	2	2
Total volumes				
Additionally added H ₂ O / mL				0.5
Total glacial acid / mL	3	3	3	3
Total solution volume / mL	19.630	19.630	19.630	20.130

Key: TIP=titanium (IV)-isopropoxide

PVP=polyvinylpyrrolidone (M_w = 1 300 000)

Ti0 = no titanium; Ti5 = 5 mol % Ti; Ti10 = 10 mol % Ti; Ti100 = no iron

Table 2

Unit-cell parameters of prepared samples calculated by program Match!

Sample	a / Å	c / Å	V / Å ³	Crystallite size* / Å
Ti0	5.0361	13.756	302.16	1067
Ti5	5.0327	13.751	301.65	439
Ti10	5.0306	13.750	301.37	359

*Crystallite sizes were estimated by Scherrer formula

Table 3⁵⁷Fe Mössbauer parameters at RT of samples Ti0, Ti5 and Ti10

Sample	Line	δ / mm s ⁻¹	Δ or E_q /mm s ⁻¹	B_{hf} / T	Γ / mm s ⁻¹	Area /%
Ti0	M	0.36	-0.22	51.0	0.21	100.0
Ti5	M	0.36	-0.20	50.8	0.24	100.0
Ti10	M	0.36	-0.20	50.6	0.25	94.2
	Q	0.34	0.91	-	0.45	5.8

Key: δ =isomeric shift relative to α -Fe at RT, B_{hf} = hyperfine magnetic field, Δ or E_q =quadrupole splitting, Γ =linewidth, M=sextet, Q=quadrupole doublet

Errors: δ and E_q or $\Delta = \pm 0.01$ mm s⁻¹, $B_{hf} = \pm 0.2$ T

Remark: Mössbauer spectra were fitted using the distribution of hyperfine magnetic fields.

Table 4

Photocatalytic efficiency of prepared samples

Sample	RhB degradation after 3h of illumination / %
Ti0	95
Ti5	28
Ti10	38
Ti100	54